Single- or Poly-Crystalline Ni-Rich Layered Cathode, Sulfide or Halide Solid Electrolyte: Which Will be the Winners for All-Solid-State Batteries?

Yoonjae Han, Sung Hoo Jung, Hiram Kwak, Seunggoo Jun, Hunho H. Kwak, Jong Hoon Lee, Seung-Tae Hong, and Yoon Seok Jung*

Two newly emerging materials for application in all-solid-state batteries, namely, single-crystalline Ni-rich layered oxide cathode and halide solid electrolyte (SE), are of utmost interest because of their superior properties (good microstructural integrity and excellent electrochemical oxidation stability, respectively) to conventional polycrystalline layered oxides and sulfide SEs. In this work, four electrodes employing single- or polycrystalline $LiNi_{0.88}Co_{0.11}Al_{0.01}O_2$ (NCA) and Li_3YCl_6 or $Li_6PS_5Cl_{0.5}Br_{0.5}$ are rigorously characterized by complementary analyses. It is shown that the synergy of employing cracking-free single-crystalline NCA and oxidation-tolerable Li_3YCl_6 can be achieved by considering intercoupled engineering factors that are prone to overlook, such as size, lightness, and mixing of particles. Accordingly, the highest level of performances in terms of discharge capacity (199 mA h g^{-1} at 0.1C), initial Coulombic efficiency (89.6%), cycling performance (96.8% of capacity retention at the 200th cycle), and rate capability (130 mA h g^{-1} at 4C) are demonstrated at 30 °C. Severe side reactions occurring at the $Li_6PS_5Cl_{0.5}Br_{0.5}$/NCA interfaces are also quantified and probed. Importantly, an overlooked but significant contribution of the side reaction of $Li_6PS_5Cl_{0.5}Br_{0.5}$ to the detrimental electrochemo-mechanical degradation of polycrystalline NCA is revealed for the first time by postmortem scanning electron microscopy and operando electrochemical pressiometry measurements.

Y. Han, Dr. S. H. Jung, H. Kwak, S. Jun, Prof. Y. S. Jung
Department of Chemical and Biomolecular Engineering
Yonsei University
Seoul 03722, Republic of Korea
E-mail: yoonsjung@yonsei.ac.kr

Y. Han, H. Kwak
Department of Energy Engineering
Hanyang University
Seoul 04763, Republic of Korea

Dr. H. H. Kwak, Prof. S.-T. Hong
Department of Energy Science and Engineering
Daegu Gyeongbuk Institute of Science and Technology (DGIST)
Daegu 42988, Republic of Korea

Dr. J. H. Lee
UNIST Central Research Facilities (UCRF)
Ulsan National Institute of Science and Technology (UNIST)
Ulsan 44919, Republic of Korea

The ORCID identification number(s) for the author(s) of this article can be found under https://doi.org/10.1002/aenm.202100126.

DOI: 10.1002/aenm.202100126

1. Introduction

Beyond its success for portable electronic devices, lithium-ion battery (LIB) technology has been extended to battery-driven electric vehicles.[1,2] Unfortunately, the current technology relying on conventional organic liquid electrolytes (LEs) has faced formidable challenges in terms of high energy density and safety, which are associated with the inherently limiting properties of LEs; flammability and incompatibility with Li metal anodes.[2–4] All-solid-state Li batteries (ASLBs) employing inorganic solid electrolytes (SEs) have thus attracted much attention.[1,5–10] Sulfide SE materials, owing to their high ionic conductivities (e.g., $Li_{5.5}PS_{4.5}Cl_{1.5}$:[11,12] 12 mS cm^{-1}), reaching those of LEs ($\approx 10^{-2}$ S cm^{-1}),[13] and mechanical sinterability, enabling simple cold-pressing-based fabrication of ASLBs,[8,14] are considered as the key to practical ASLB technology. However, their several critical disadvantages of chemical and electrochemical instabilities have been serious obstacles.[8,15–18] Upon exposure to humid air, sulfide SE materials release toxic H_2S gas,[8,19,20] requiring strict dry-room conditions for manufacturing processes, which are translated into high manufacturing costs. Moreover, they exhibit poor intrinsic electrochemical oxidation stability (<3 V vs Li/Li+).[8,21,22]

Li metal is an ideal anode that is hoped to be enabled by the development of all-solid-state technologies.[3,23–29] Ni-rich layered oxides, $LiMO_2$ (M = Ni, Co, Mn, Al), which have been extensively investigated as cathodes for advanced LIBs based on LEs,[30–36] are also strong candidates for integration into practical ASLBs at scale.[18,37,38] Despite the use of SEs showing high Li+ conductivities (>10^{-3} S cm^{-1}), electrochemical performances of layered oxide cathodes including $LiCoO_2$ and $Li[Ni,Co,Mn]O_2$ in ASLB cells have not been satisfactorily high in most previous reports.[8,39–42] Along with the intrinsically low electrochemical oxidation stability of sulfide SEs, their chemically reactive feature in contact with layered oxide cathodes, which is more severe for high-energy targeted Ni-richer $Li[Ni,Mn,Co]O_2$, is the main cause for their low electrochemical

**ADVANCED
SCIENCE NEWS**
www.advancedsciencenews.com

**ADVANCED
ENERGY
MATERIALS**
www.advenergymat.de

performance.[15,22,37,43,44] This problem has been partly addressed by the development of protective coatings, such as $LiNbO_3$,[5] $Li_4Ti_5O_{12}$,[45] $Li_{3-x}B_{1-x}C_xO_3$,[46] TaO_3,[47] Al_2O_3,[48] and Li_2ZrO_3.[26] Moreover, sulfide SEs in contact with an inactive component of conductive carbon additives are oxidatively decomposed at the entire range of operating voltages of $Li[Ni,Mn,Co]O_2$, leading to the lowered initial Coulombic efficiency (ICE) and gradual capacity fading upon cycling.[49]

Owing to the incompressible feature of SEs, electrochemo-mechanical effects on the performance are also critical for all-solid-state batteries.[37,50,51] Even slight volumetric strains of a few percentages in $LiMO_2$ during charge and discharge induces loosening and/or loss of interfacial ionic contacts.[18,37,38,52] Moreover, very recently, our group demonstrated that commercial-grade $LiNi_{0.80}Co_{0.10}Mn_{0.10}O_2$, consisting of randomly oriented grains, was susceptible to severe disintegration of the secondary particles even at the initial charge and discharge due to the anisotropic volumetric strains, which led to poor electrochemical performance of low ICE and degradation of cycling retention.[37] In this regard, recently emerging research directions for cathodes in advanced LIBs based on LEs, the development of cracking-free single-crystalline Ni-rich layered oxides,[30,53–58] could be in the same vein for the development of practical ASLBs.

The recent discovery of halide SEs (Li_3YX_6 (X = Cl, Br)) with Li^+ conductivities of over 10^{-4} S cm^{-1} has opened new opportunities due to their excellent electrochemical oxidation stability (>4 V vs Li/Li^+) and much better chemical stability (more oxygen-resistant and no H_2S evolution), compared to sulfide SEs, as well as deformability.[59,60] By exploration of the Li_3YX_6 analogs, highly Li^+ conductive halide SEs of Li_3InCl_6 (1.5 mS cm^{-1}),[61] Li_3ErCl_6 (0.33 mS cm^{-1}),[62] Li_3ScCl_6 (3.0 mS cm^{-1}),[63,64] and $Li_{3-x}M_{1-x}Zr_xCl_6$ (M = Y, Er, 1.4 mS cm^{-1}),[65] $Li_{2+x}Zr_{1-x}Fe_xCl_6$ (max. ≈ 1 mS cm^{-1})[66] were identified. By employing these new halide SEs, uncoated $LiCoO_2$ electrodes showed good electrochemical performance, which was attributed to their high electrochemical oxidation stability.[65,66,67] To date, reports on the application of halide SE for Ni-rich layered oxides are scarce.[64,66]

The aforementioned advances in understanding the failure modes of Ni-rich layered oxides in terms of electrochemical and electrochemo-mechanical stabilities, advanced Ni-rich layered oxides with electrochemo-mechanically compliant microstructures, and new halide SEs led us, herein, to the rigorous investigation of all-solid-state cells with variations in Ni-rich layered oxides (single-crystalline $LiNi_{0.88}Co_{0.11}Al_{0.01}O_2$ (single-NCA) vs conventional polycrystalline $LiNi_{0.88}Co_{0.11}Al_{0.01}O_2$ (poly-NCA)) and SEs (halide SE Li_3YCl_6 (LYC) vs conventional sulfide SE $Li_6PS_5Cl_{0.5}Br_{0.5}$ (LPSX)). Notably, several critical counteracting pros and cons of two sets of NCAs and SEs, summarized in **Figure 1**a, pose intriguing questions on the type of factors that are critical from the viewpoint of designing ASLBs. First, compared to poly-NCA, single-NCA shows better mechanical integrity but smaller particle sizes.[53,56] Second, the excellent electrochemical oxidation stability of LYC, compared with LPSX, should be offset by an order of magnitude lower Li^+ conductivity of 0.40 mS cm^{-1} at 30 °C (vs 4.8 mS cm^{-1} for LPSX) as well as higher specific density of 2.43 g cm^{-3} for LYC (vs 1.96 g cm^{-3} for LPSX).

Four electrodes of S/LYC, P/LYC, S/LPSX, and P/LPSX (e.g., S/LYC refers to a composite electrode consisting of single-NCA and LYC) in all-solid-state cells were thus extensively characterized. The employment of single-NCA and halide SE LYC, that is S/LYC, shows the best ICE (87.7%) and cycling performances, but still with gradual capacity fading, showing ≈67.2% capacity retention at the 200th cycle. Postmortem cross-sectional scanning electron microscopy-backscattered electron (SEM-BSE) measurements revealed that the inhomogeneous distribution of single-NCA in the S/LYC electrode, stemming from the smaller particle size of single-NCA and higher specific density of LYC, compared to poly-NCA and LPSX, respectively, are responsible for the unsatisfactory cycling retention. The capacity retention of the S/LYC electrode was dramatically improved by adding a larger amount of LYC (from 29.1 to 40.7 wt%) to 96.8% at the 200th cycle, which is at an unprecedented level in this field. Notably, with the aid of operando electrochemical pressiometry measurements for the P/LYC and P/LPSX electrodes as well as RuO_2/LPSX and C/LPSX electrodes, detrimental electrochemo-mechanical effects by the side reaction of LPSX on the performance of NCA in all-solid-state cells have also been demonstrated for the first time. Moreover, complementary analysis by in situ and ex situ X-ray diffraction (XRD), ex situ transmission electron microscopy (TEM), and ex situ X-ray photoelectron spectroscopy (XPS) measurements provides a solid understanding of the degradation modes of the NCA electrodes in ASLBs.

2. Results and Discussion

Single- and poly-crystalline NCA particles (single-NCA and poly-NCA) were used without any coatings. The chemical composition of $Li[Ni_{0.88}Co_{0.11}Al_{0.01}]O_2$ was confirmed by inductively coupled plasma optical emission spectroscopy (ICP-OES) measurements. Their single- and poly-crystalline features are observed in the SEM images in Figure S1a–d in the Supporting Information. The particle sizes of single-NCA (D_{50} = 2.8 µm) are smaller than those of poly-NCA (D_{50} = 11.9 µm) (Figure S1e,f, Supporting Information), which is consistent with the larger surface area (Figure S2, Supporting Information). Rietveld refinement of the XRD results showed marginal differences in lattice parameters with identical crystal structure of space group $R\bar{3}m$ (Figure S3 and Table S1, Supporting Information).[37] Residual Li surface impurities on both NCAs (Table S2, Supporting Information) were measured to be much lower than in previous literature,[68] indicating their minimal effects on the electrochemical performance of all-solid-state cells.

Two types of SE were used for the NCA electrodes, LYC (Li_3YCl_6) and LPSX ($Li_6PS_5Cl_{0.5}Br_{0.5}$). They showed a difference of an order of magnitude in Li^+ conductivities at 30 °C, 0.40 mS cm^{-1} for LYC, and 4.8 mS cm^{-1} for LPSX (the Arrhenius plots of Li^+ conductivity are provided in Figure S4 in the Supporting Information). Their XRD patterns (Figure S5, Supporting Information) agree well with previous reports, indicating that LYC belongs to a hexagonal closed-packed (hcp) crystal structure with the space group $P\bar{3}m1$ despite the low crystallinity,[59] while LPSX has a face-centered-cubic (fcc) crystal structure with the space group $F\bar{4}3m$.[11] Their SEM images for

ADVANCED
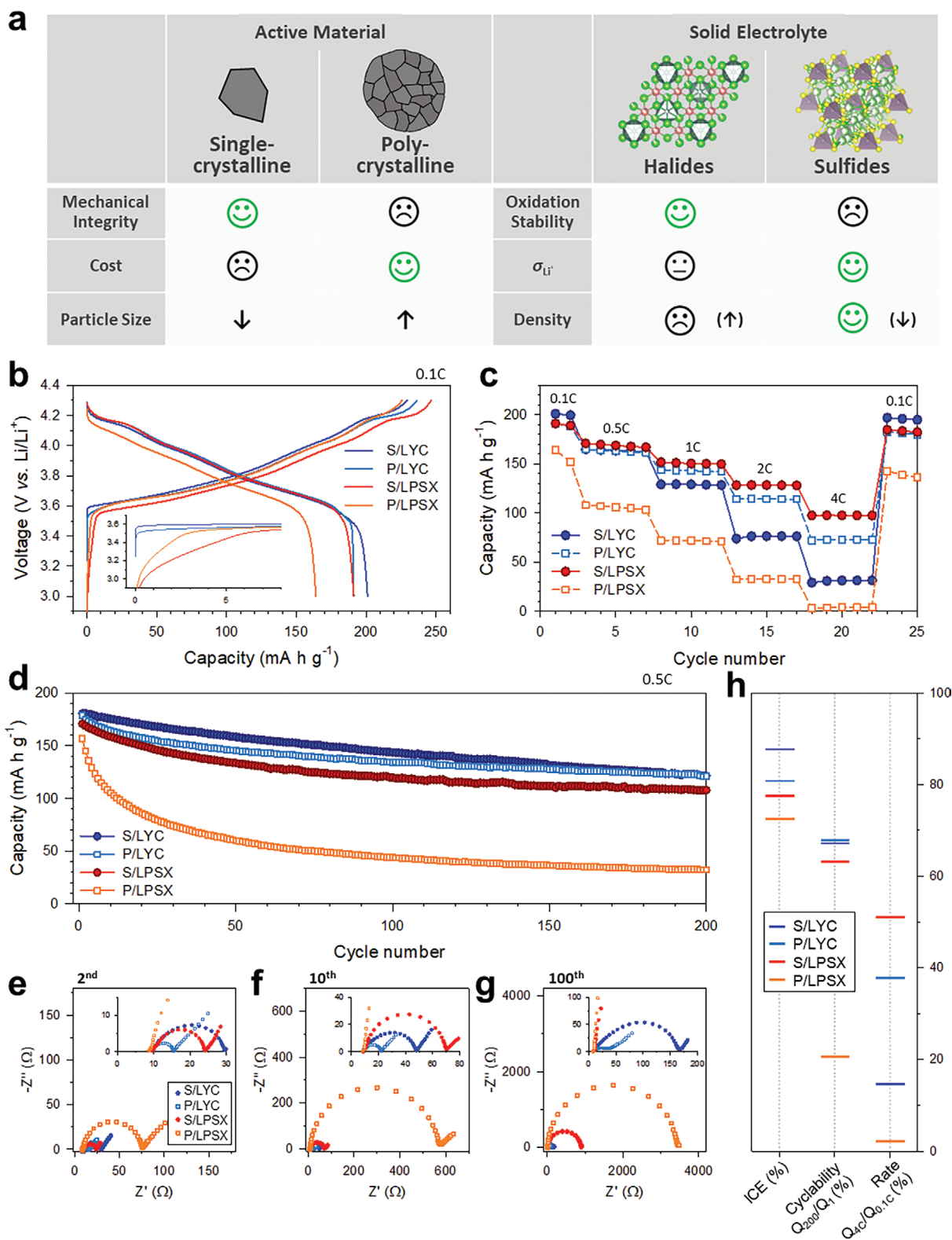**SCIENCE NEWS**
www.advancedsciencenews.com

ADVANCED
ENERGY
MATERIALS
www.advenergymat.de

Figure 1. Comparative electrochemical results of electrodes employing single- or poly-crystalline NCA ($LiNi_{0.88}Co_{0.11}Al_{0.01}O_2$) with halide (LYC ($Li_3YCl_6$)) or sulfide (LPSX ($Li_6PS_5Cl_{0.5}Br_{0.5}$)) SEs in all-solid-state half cells at 30 °C. a) Pros and cons for Ni-rich layered oxides (single- vs poly-crystalline) and SEs (halides vs sulfides). b) First-cycle charge–discharge voltage profiles at 0.1C and 30 °C for electrodes with four different combinations of NCA (single- or poly-crystalline) and SEs (LYC or LPSX) and their corresponding c) rate and d) cycling performances at 0.5C. Nyquist plots for the electrodes at the e) 2nd, f) 10th, and g) 100th cycles. h) Comparative results of cell performances of the electrodes.

particles and cold-pressed pellets (Figure S6a–d, Supporting Information) show the excellent deformability. Also, their particle sizes (≈4 µm, Figure S6e,f, Supporting Information) are similar, and hence, the size effect on cell performance could be ruled out.[69]

Four mixture electrodes of S/LYC, P/LYC, S/LPSX, and P/LPSX were prepared by manual mixing of NCA (single-NCA or poly-NCA), SE (LYC or LPSX), and carbon additives in a weight ratio of 70:30:3, and tested using NCA/Li-In all-solid-state half cells at 30 °C. The performance trends might be predicted to some extent by the complementary consideration of several factors: the microstructure and size for NCA; and the electrochemical oxidation stability, Li$^+$ conductivity, and lightness, for SEs, as illustrated in Figure 1a. In particular, the cyclability of S/LYC electrodes in all-solid-state cells was expected to be the best.

The electrochemical performances of the four electrodes cycled between 3.0 V and 4.3 V (vs Li/Li$^+$) at 30 °C are compared in Figure 1b–h and Table S3 (Supporting Information). First-cycle charge–discharge voltage profiles at 0.1C are shown in Figure 1b. Variations in first-cycle charge capacities despite the identical composition of Li[Ni$_{0.88}$Co$_{0.11}$Al$_{0.01}$]O$_2$ implies complicated contributions of side reactions occurring at the LPSX/NCA interfaces and detrimental electrochemo-mechanical evolution that is severe for poly-NCA.[37,52] Notably, the sloping charge voltage profiles of the electrodes using LPSX (S/LPSX and P/LPSX), starting at ≈3 V (vs Li/Li$^+$), in the enlarged view in the inset of Figure 1b, clearly indicate severe side reactions.[49] Self-discharge tests also confirmed much more severe side reactions in the electrode employing LPSX (P/LPSX) than in the electrode employing LYC (P/LYC) (Figure S7, Supporting Information). For the first discharge capacity, the result of the highest value for S/LYC (201 mA h g^{-1}) and the lowest value for P/LPSX (164 mA h g^{-1}) is in good agreement with our prediction based on the good electrochemical stability of LYC and the electrochemo-mechanically compliant microstructure of single-NCA. These factors are also well reflected by the ICE values in the descending order of S/LYC (87.7%) > P/LYC (80.8%) > S/LPSX (77.5%) > P/LPSX (72.5%), as summarized in Figure 1h. However, in terms of the rate capability trend, shown in Figure 1c, the consideration of Li$^+$ conductivity (one order of magnitude higher for LPSX (4.8 mS cm^{-1}) than for LYC (0.40 mS cm^{-1})) should be amended. The performances in terms of rate capability can be expressed as S/LPSX > P/LYC > S/LYC > P/LPSX, and thus, the best performance is by using LPSX (S/LPSX).

Cycling performance and its corresponding CE results at 0.5C are displayed in Figure 1d and Figures S8 and S9 (Supporting Information). The capacity retention shows a descending order of S/LYC ≈ P/LYC > S/LPSX >> P/LPSX. This is also in good agreement with the trend in the interfacial resistances corresponding with the amplitudes of the semicircles in the Nyquist plots (Figure 1e–g) obtained by electrochemical impedance spectroscopy (EIS) measurements (the fitted results are shown in Figure S10 and Table S4 in the Supporting Information).[37,40,46] Notably, the distinctly fastest capacity fading of P/LPSX (Figure 1d) is in line with the results of the first-cycle discharge capacity (Figure 1b), rate capability (Figure 1c), and the ICE, and it clearly indicates the detrimental effects of both the cracking-prone polycrystalline microstructure of poly-NCA and

the severe side reaction at LPSX/NCA interfaces. Interestingly, we have been puzzled by the fact that the cycling performance of S/LYC (67.2% capacity retention at the 200th cycle) appeared comparable to that of P/LYC (67.8%) (Figure 1d), and the evolution of the overpotential of S/LYC upon cycling was also slightly faster than that of P/LYC (Figures S11, and S12, Supporting Information). This result may be in line with the higher rate capability of P/LYC than that of S/LYC (Figure 1c), which could also be abnormal as the single-NCA showed a smaller particle size than that of poly-NCA, and thus, had a shorter Li$^+$ diffusion length.[70]

Microstructural evolution in composite electrodes was characterized by cross-sectional SEM-BSE measurements, as displayed in **Figure 2**. The images are shown for the samples before cycling (Figure 2a–d), after the first charge to 4.3 V (vs Li/Li$^+$) (Figure 2e–h) and the subsequent discharge to 3.0 V (vs Li/Li$^+$) (Figure 2i–l), and after 100 cycles (Figure 2m–p). Moreover, quantitative analysis results on the microcracks for the poly-NCA electrodes (P/LYC and P/LPSX) are summarized in **Figure 3** and Figures S13 and Table S5 (Supporting Information). After the first charge, no significant change was observed for the electrodes using single-NCA (S/LYC (Figure 2e) and S/LPSX (Figure 2g)). In contrast, poly-NCA particles in the P/LYC and P/LPSX electrodes (Figure 2f,h, respectively) clearly showed internal cracks, which are the result of lattice shrinkage, especially associated with the deleterious H2–H3 phase transition at >≈4.1 V (vs Li/Li$^+$).[32–34,52] Interestingly, the formation of internal cracks was more severe for the electrodes with LYC than with LPSX, as confirmed by the quantitative analysis results of the microcrack (3.93% and 3.69% for P/LYC and P/LPSX, respectively, Table S5 (Supporting Information), Figure 3c). This may indicate more shrinkage of grains in poly-NCA due to the higher state-of-charge (SOC) of NCA with LYC than with LPSX, which could be caused by less polarization.[32–34] This issue is discussed later.

After the first discharge, the S/LYC electrodes showed noticeable internal cracks in single-NCA (Figure 2i), whereas no internal cracks were observed for single-NCA in combination with LPSX (S/LPSX) (Figure 2k). First, we considered whether this result may originate from the different mechanical properties of the two SEs. Thus, their deformability was assessed by measuring the Li$^+$ conductivity and porosity of the SE pellets as a function of the applied pressure (Figure S14, Supporting Information). At a cell fabrication pressure of 370 MPa, however, LYC showed a similar saturated Li$^+$ conductivity and porosity, compared to LPSX. Therefore, the effect of different mechanical properties of SEs could be ruled out to account for the formation of internal cracks in single-NCA for S/LYC. Then, the density difference of the SEs (2.43 g cm^{-3} for LYC and 1.96 g cm^{-3} for LPSX), was suspected as the same weight fraction of SEs in the electrodes is translated into the smaller volume fraction of LYC than that of LPSX. Indeed, the single-NCA particles were not covered by LYC well and aggregated with each other (Figure 2a,e,i). Moreover, the internal cracks were distinct for the aggregated single-NCA particles (Figure 2i), indicating that the compressive stresses applied between the brittle single-NCA particles in the absence of ductile SE is responsible for the internal cracks.[50,71] In contrast, single-NCA particles in S/LPSX remained intact with better
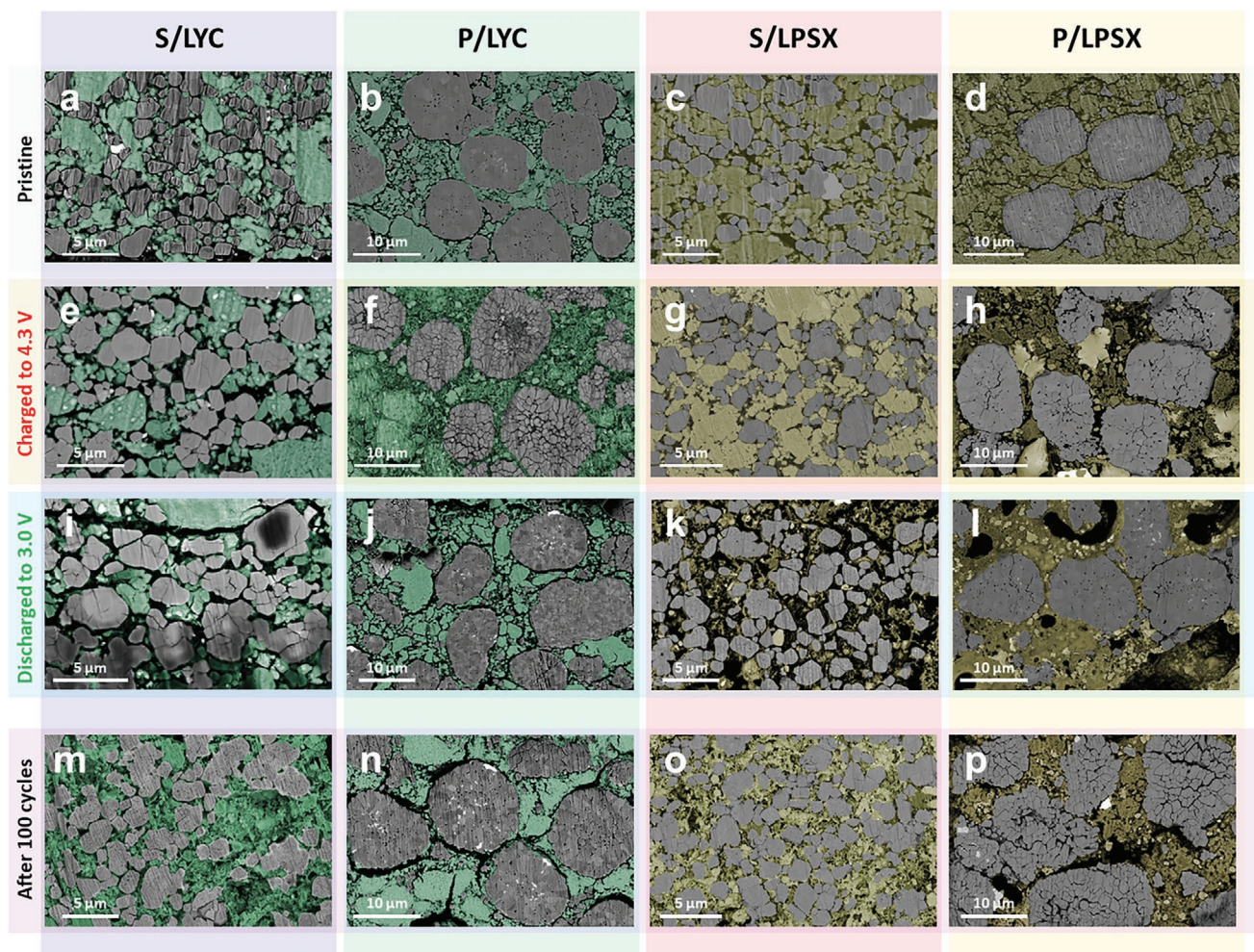
Figure 2. Cross-sectional SEM-BSE images of the electrodes employing single- or poly-crystalline NCA with halide (LYC) or sulfide (LPSX) SEs before and after cycling. Cross-sectional SEM-BSE images of the four electrodes a–d) before cycling and after e–h) first charge to 4.3 V (vs Li/Li$^+$) and i–l) subsequent discharge to 3.0 V (vs Li/Li$^+$), and m–p) after 100 cycles.

spatial distribution (Figure 2k), which could be due to the larger volume fraction of LPSX, compared to that of LYC in S/LYC. Furthermore, even poly-NCA showed marginal internal cracks in P/LYC (Figure 2j). Compared to single-NCA in S/LYC, poly-NCA in P/LYC formed better surface coverage by LYC, which is attributed to the larger particle sizes of poly-NCA than those of single-NCA. These observations indicate that the single-NCA in S/LYC suffered from internal cracking because of their poor spatial distribution, which is the result of high specific density of LYC and the small particle size of single-NCA. NCA particles, which are in poor contact with LYC and instead touch neighboring NCA particles in S/LYC, would thus be more vulnerable to the loss or loosening of ionic contacts upon volumetric strains upon charge and discharge. This could be responsible for the below-par performance of S/LYC with 29.1 wt% LYC.

In this regard, the S/LYC electrodes were tested with an excessive amount of LYC, 40.7 wt% (the weight ratio of NCA to LYC to carbon was 70:50:3), where the surface coverage of single-NCA by the SE LYC was significantly increased (**Figure 4**; Table S6, Supporting Information). Corresponding Coulombic efficiency results are shown in Figure S15 in the Supporting

Information. In the cross-sectional SEM-BSE image, the S/LYC electrode with 40.7 wt% LYC was free from internal cracks (Figure 4b) in contrast to the electrode with 29.1 wt% LYC (Figure 4a or Figure 2c). Accordingly, the cycling performance was dramatically improved by the application of excessive LYC, from 67.2% of capacity retention at the 200th cycle to 89.3%, and even to 96.8% when no constant voltage mode was applied (Figure 4c). To the best of our knowledge, this is far superior to other conventional LIBs and ASLBs when bare LiMO$_2$ is utilized. Indeed, S-NCA paired with 40.7 wt% LYC showed much higher capacity retention (96.8% after 200 cycles), as compared to that with conventional liquid electrolytes (68.4%) (Figure 4c), which sheds light on promising opportunity of the all-solid-state technology. Capacity fading of conventional NCM (or NCA)/Li half cells using LEs is attributed to the degradation of not only cathode but also Li metal anode. Specifically, cross-over of transition metal ions dissolved from NCA cathode to Li metal anode is detrimental.[72] In this regard, the absence of the "cross-talk" problem for ASLBs is also an important advantage.

The rate capability for S/LYC with 40.7 wt% LYC was also far superior to that with 29.1 wt%; 130 mA h g^{-1} versus 32 mA h g^{-1}

**ADVANCED
SCIENCE NEWS**

www.advancedsciencenews.com

**ADVANCED
ENERGY
MATERIALS**
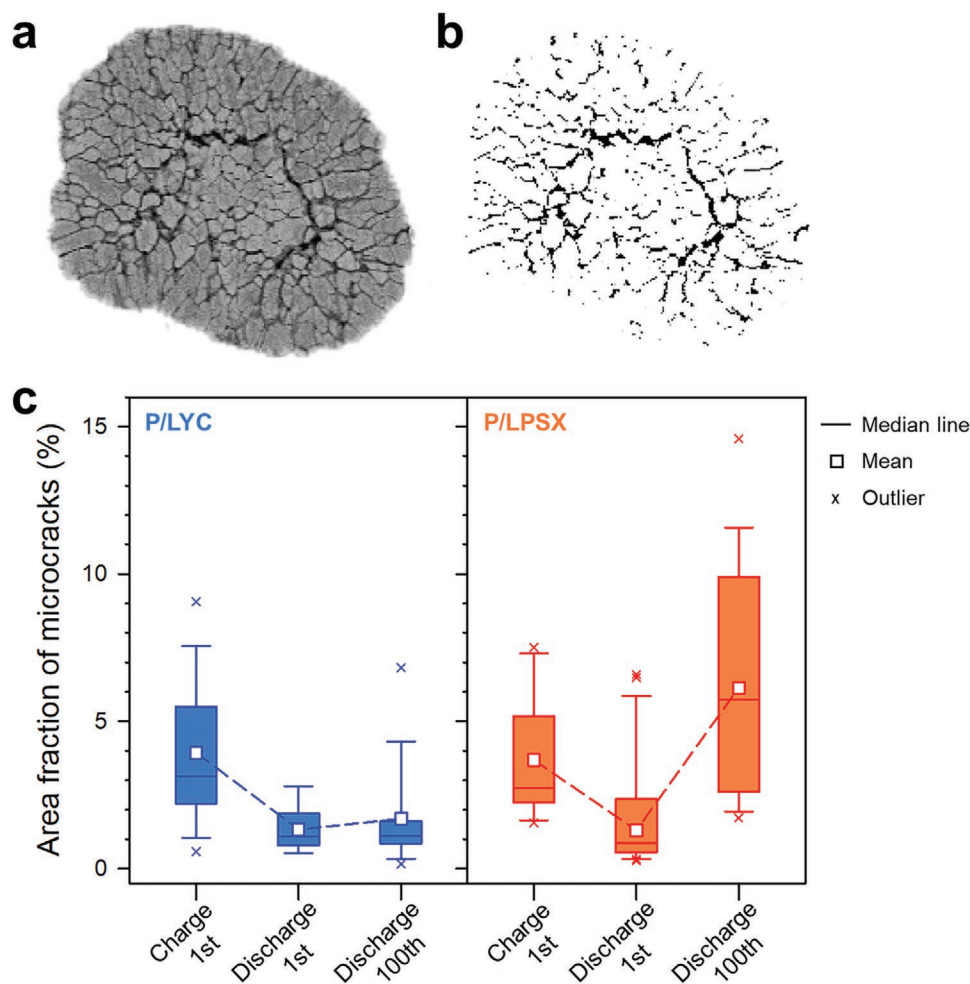
www.advenergymat.de

Figure 3. Quantitative analysis results of microcracks in poly-NCA particles in P/LYC and P/LPSX electrodes. a) Typical SEM-BSE image of a poly-NCA particle and b) its corresponding microcracks. c) Box plot of the area fraction of microcracks of poly-NCA for the P/LYC and P/LPSX electrodes after first charge to 4.3 V (vs Li/Li$^+$) and subsequent discharge to 3.0 V (vs Li/Li$^+$), and after 100 cycles. Analysis results are summarized in Table S5 in the Supporting Information.

at 4C (Figure 4d), which is also consistent with the EIS results shown in Figure 4e–g and Table S7 (Supporting Information). These results clearly verify our hypothesis on the origin of the unsatisfactory cycling performance of the S/LYC electrode with 29.1 wt% LYC: the detrimental electrochemo-mechanical effect due to the poor spatial distribution of single-NCA that stems from the heavy LYC and the small single-NCA. In contrast, the P/LYC and S/LPSX electrodes did not show noticeable improvements in cycling and rate performances by adding an excessive amount of SE (40.7 wt%) (Figures S16 and S17, Supporting Information). The major reason for capacity fading in these electrodes was thus not the poor spatial distribution of cathode active materials but the disintegration of poly-NCA and the severe interfacial side reaction for the P/LYC and S/LPSX electrodes, respectively.

Interestingly, high-magnification SEM-BSE images for S/LYC and P/LYC after first cycle and first charge, respectively, reveal the creation of fine cracks at the nanoscale within grains (Figures S18 and S19, Supporting Information). This would be in line with a recent report showing the reversible evolution of

microcracks of single-crystalline Ni-rich cathode materials in conventional liquid electrolyte cells.[57]

The detrimental electrochemo-mechanical effects, reflected by the internal cracks in poly-NCA and the gaps between NCAs and SEs, became more obvious for the electrodes after 100 cycles (Figure 2m–p). As expected, regardless of the SE, single-NCA particles maintained their overall structural integrity even after 100 cycles. Interestingly, for poly-NCA, the secondary particles shattered much more severely for the P/LPSX electrode (Figure 2p), compared to those for the P/LYC electrode (Figure 2n), which is also in line with the cycling performance results (Figure 1d). The area fraction of the microcracks for P/LYC and P/LPSX after 100 cycles was 1.69% and 6.14%, respectively (Table S5 (Supporting Information), Figure 3c). This result strongly suggests an overlooked contribution of LPSX-related side reactions to the electrochemo-mechanical effect. The volumetric strain caused by the side reaction of LPSX was assessed for the poly-NCA electrodes using LPSX, in comparison with using LYC, in all-solid-state cells using zero-strain Li$_4$Ti$_5$O$_{12}$ counter electrodes (**Figure 5**a,b). The first-cycle

ADVANCED
SCIENCE NEWS
www.advancedsciencenews.com

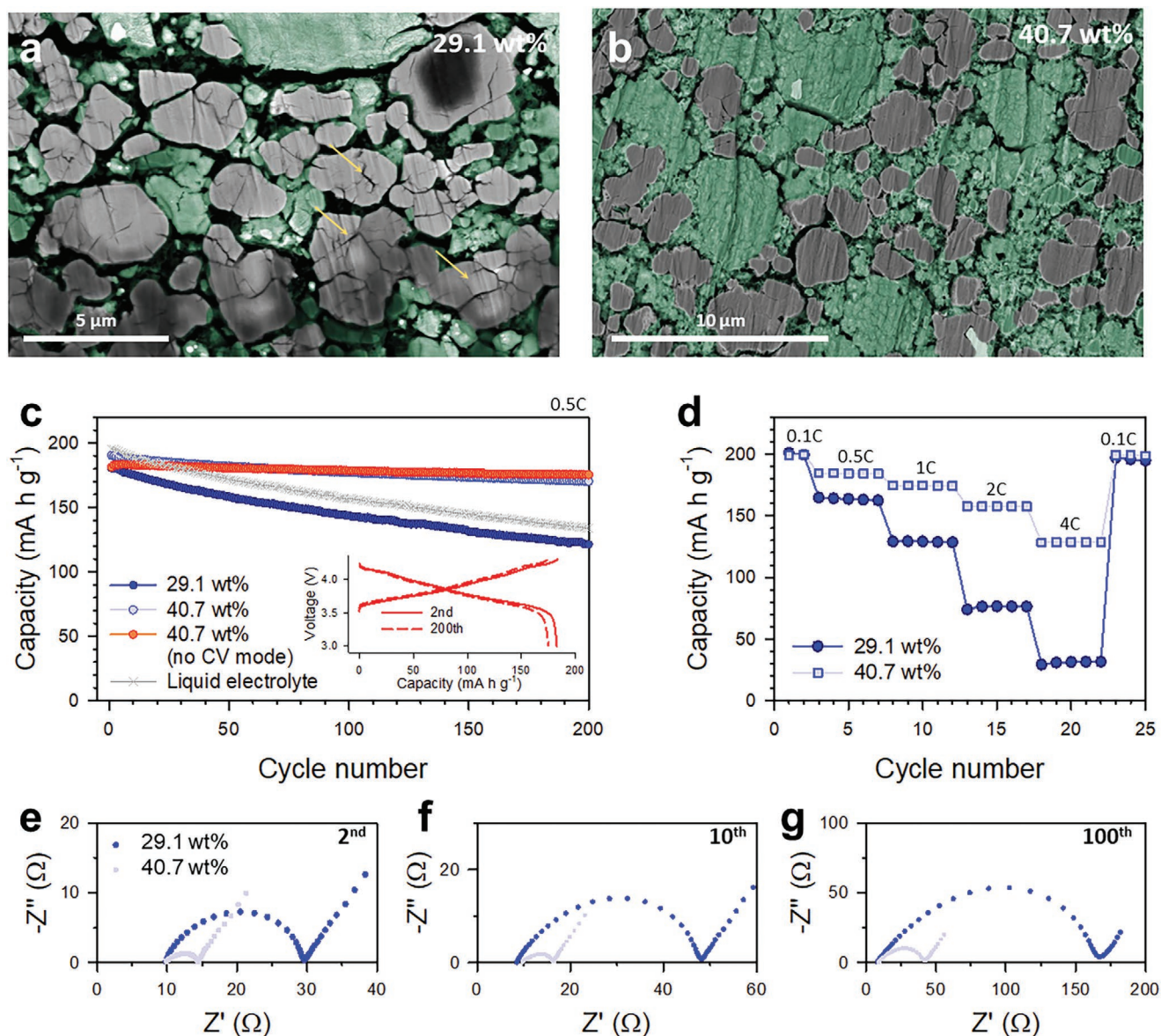ADVANCED
ENERGY
MATERIALS
www.advenergymat.de

Figure 4. Results of S/LYC electrodes with an excessive amount of LYC (40.7 wt%) for all-solid-state half cells tested at 30 °C. Cross-sectional SEM-BSE images of S/LYC electrodes with a) 29.1 wt% and b) 40.7 wt% LYC after first discharge to 3.0 V (vs Li/Li$^+$). Note the cracks formed inside the single-NCA, indicated by the arrows in (a). c) Cycling performances at 0.5C for the S/LYC electrodes with varied amounts of LYC. The cells were charged with or without CC–CV (constant current–constant voltage) mode. In the inset, the charge–discharge voltage profiles at the 2nd and 200th cycles for S/LYC with 40.7 wt% LYC are shown. A result for S-NCA electrodes in liquid electrolyte cells is also compared. d) Rate capabilities and Nyquist plots at the e) 2nd, f) 10th, and g) 100th cycles for the S/LYC electrodes with varied amounts of LYC.

charge voltage profile, and corresponding pressure change and capacity-derivative pressure curves are shown in Figure 5b. In contrast to the poly-NCA employing LYC electrode, the poly-NCA electrode employing LPSX exhibited an abrupt pressure decrease at the very beginning of the first-cycle charge (highlighted in green), where the side reaction dominates over Li$^+$ deintercalation out of NCA (in the middle of Figure 5b). This feature is more evident in the capacity-derivative differential pressure (or differential electrochemical pressiometry (DEP)) curve (at the bottom of Figure 5b). Moreover, the minimum point for the DEP profile of P/LPSX, which can be regarded as the indicator of SOC,[51] is shifted toward a positive direction

(indicated by an arrow), as compared to that of P/LYC, reflecting a delayed charge (or Li$^+$ deintercalation) for P/LPSX due to the severe side reaction of LPSX.

To further clarify the contribution of LPSX-related side reaction to the electrochemo-mechanical evolution, RuO$_2$/LPSX composite electrodes were prepared and characterized by electrochemical pressiometry (Figure 5a,d; Figure S20a, Supporting Information), ex situ XPS (Figure 5c), and cross-sectional SEM-BSE measurements (Figure 5e,f; Figures S20b,c and S21, Supporting Information). Because RuO$_2$ is Li$^+$-inactive in the operational voltages of NCA and electronically conductive, it could act as a good model compound that induces SE

**ADVANCED
SCIENCE NEWS**

www.advancedsciencenews.com

**ADVANCED
ENERGY
MATERIALS**
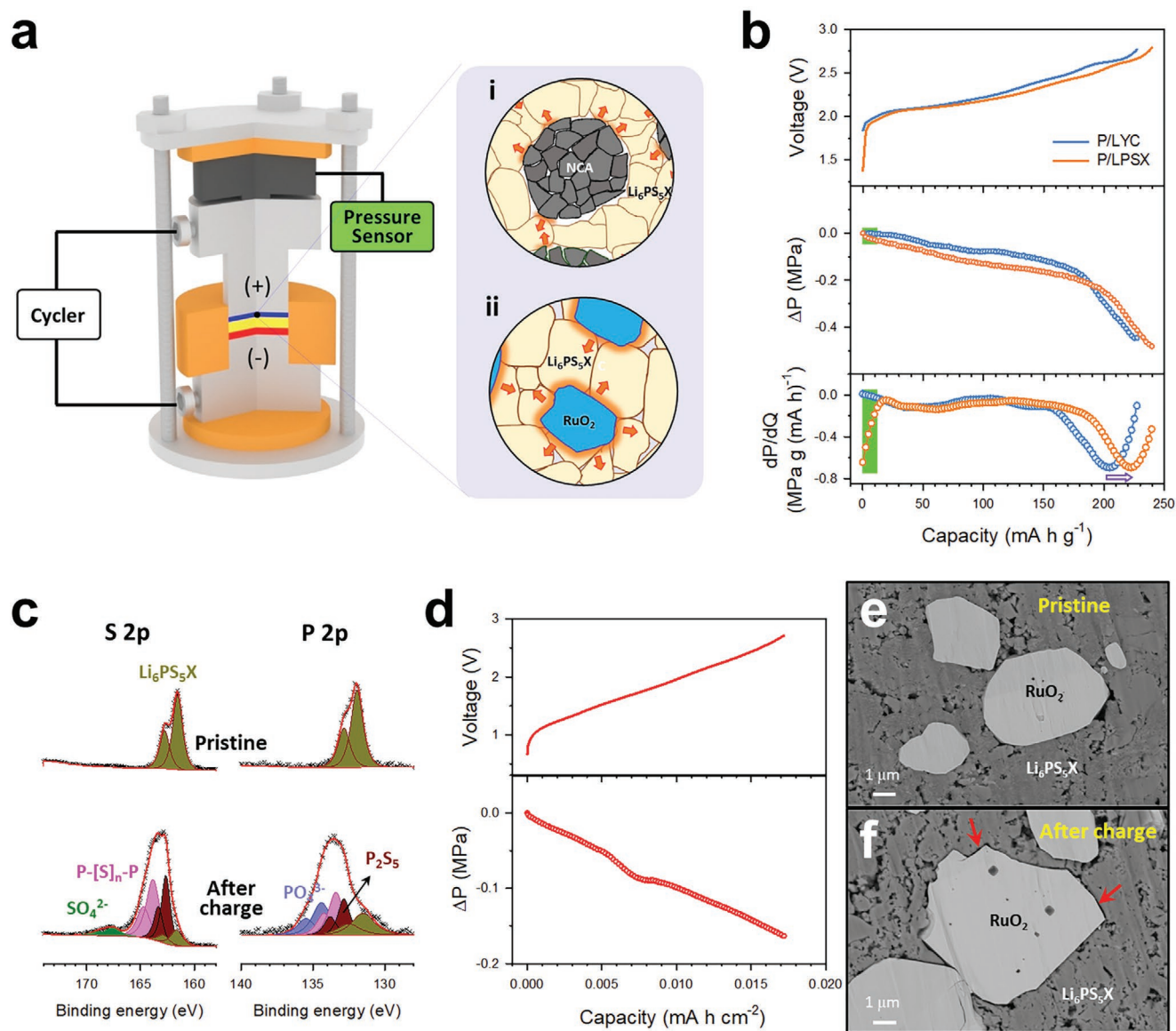
www.advenergymat.de

Figure 5. Results of electrochemo-mechanical evolution, driven by the side reaction of SE (LPSX), for poly-NCA electrodes employing LPSX or LYC, and RuO₂/LPSX electrodes in all-solid-state cells at 30 °C. a) Schematic illustrating pressure monitoring all-solid-state cells for poly-NCA electrode employing i) LPSX, where the localized stresses caused by the side reaction of LPSX at the interfaces (indicated by arrows) are shown. ii) Illustration for micro-RuO₂/LPSX electrode. Zero-strain Li₄Ti₅O₁₂ were used for counter electrodes. b) First-cycle charge voltage profiles and corresponding pressure change (and DPE profiles) for poly-NCA electrodes employing LYC or LPSX. c) Ex situ XPS spectra for micro-RuO₂/LPSX electrodes before cycling and after charge to 4.3 V (vs Li/Li⁺). d) First-cycle charge voltage profiles and corresponding pressure change for RuO₂/LPSX electrodes. Cross-sectional SEM-BSE images of micro-RuO₂/LPSX electrodes e) before cycling and f) after charge to 4.3 V (vs Li/Li⁺). Note the gap at the RuO₂-LPSX interfaces, indicated by arrows in (f).

decomposition without any effect related to Li⁺ insertion/deinsertion.[73,74] Therefore, the contribution of LPSX-related side reaction to the electrochemo-mechanical effect could be extracted. Furthermore, the size of RuO₂ particles could be controlled by further heat-treatment. While as-obtained RuO₂ is nanosized (<≈100 nm), sintering at 1050 °C for 24 h in air resulted in microsized RuO₂ (>≈1 μm). Hereafter, they are referred to as nano- and micro-RuO₂, respectively. Ex situ XRD patterns of the RuO₂/LPSX electrodes showed no changes after charge, as compared to the pristine sample, confirming

the intactness of RuO₂ in terms of Li⁺ insertion/deinsertion (Figure S22, Supporting Information).[73,74] The severe side reaction of LPSX in the RuO₂/LPSX electrodes charged to 4.3 V (vs Li/Li⁺) was confirmed by the ex situ XPS result (Figure 5c), where signals of LPSX-derived oxidized species, such as P₂S₅, bridging sulfur species, phosphates, and sulfates, were confirmed.[37,42,46,66,75] Specifically, the formation of phosphates and sulfates indicates that oxygen in RuO₂ was involved in the side reaction, which is in common with the NCA/LPSX electrodes.[37,42,46,66,75] Importantly, the distinct pressure decreases

**ADVANCED
SCIENCE NEWS**

www.advancedsciencenews.com

**ADVANCED
ENERGY
MATERIALS**

www.advenergymat.de

upon charge (or oxidation of LPSX) were revealed in the oper-ando electrochemical pressiometry results for the both micro-RuO_2/LPSX and nano-RuO_2/LPSX electrodes in all-solid-state cells (Figure 5d; Figure S20a, Supporting Information). This result is consistent with the abrupt pressure decrease at the very beginning of the first-cycle charge for poly-NCA electrodes when using LPSX (Figure 5b) and the results for (C/LPSX)/$Li_4Ti_5O_{12}$ all-solid-state cells (Figure S23, Supporting Information). Moreover, cross-sectional SEM-BSE images of the RuO_2/LPSX electrodes after charge evidences the volumetric shrinkage of LPSX due to its oxidative decomposition at the interfaces. For micro-RuO_2/LPSX in Figure 5e,f and Figure S21 (Supporting Information), sharp void spaces between RuO_2 and LPSX are clear for the charged electrode (indicated by arrows in Figure 5f), which is contrasted by intimate contacts for the pristine sample (Figure 5e). For nano-RuO_2/LPSX in Figure S20b,c in the Supporting Information, LPSX region became porous after charge, which is also interpreted as the result of volumetric shrinkage of LPSX via the interfacial decomposition. The contribution of the side reaction to the electrochemo-mechanics was thus evidenced.

As illustrated for the poly-NCA/LPSX electrode in Figure 5a, it should be noted that the surface coverage of NCA by LPSX is inhomogeneous. LPSX would be oxidatively decomposed at the

contacting interfaces. Accordingly, the corresponding stresses should evolve in a highly localized manner. Moreover, the contacting interfaces would change dynamically upon repeated charge–discharge cycling. This dynamically changing evolution of the localized stresses, caused by the side reaction of LPSX, should thus be a major driving force for the reorganization of primary particles in poly-NCA when combined with LPSX, in other words, the disintegration of secondary particles of poly-NCA.

A remaining question is: Why does the poly-NCA in the P/LYC electrode show more severe internal cracks after the first charge (Figure 2f) than that in the P/LPSX electrode (Figure 2h) (the crack area fraction of 3.93% and 3.69%, respectively (Table S5, Supporting Information))? In situ and ex situ XRD measurements were carried out to estimate the SOCs of poly-NCAs in the P/LYC and P/LPSX electrodes. The results are shown in **Figure 6** and Figures S24–S26 (Supporting Information). The (003) peaks reflecting the lattice parameter on the c-axis were chosen as an indicator of the SOCs,[18,33,34,76,77] and their evolution during charge and discharge at the first cycle for P/LYC and P/LPSX are shown in Figure 6b,c, respectively. Furthermore, the corresponding changes in the (003) peak position, that is, $2(\theta-\theta_{pristine})$, are displayed in Figure 6d. During charge, the (003) peak position changes less for P/LPSX than
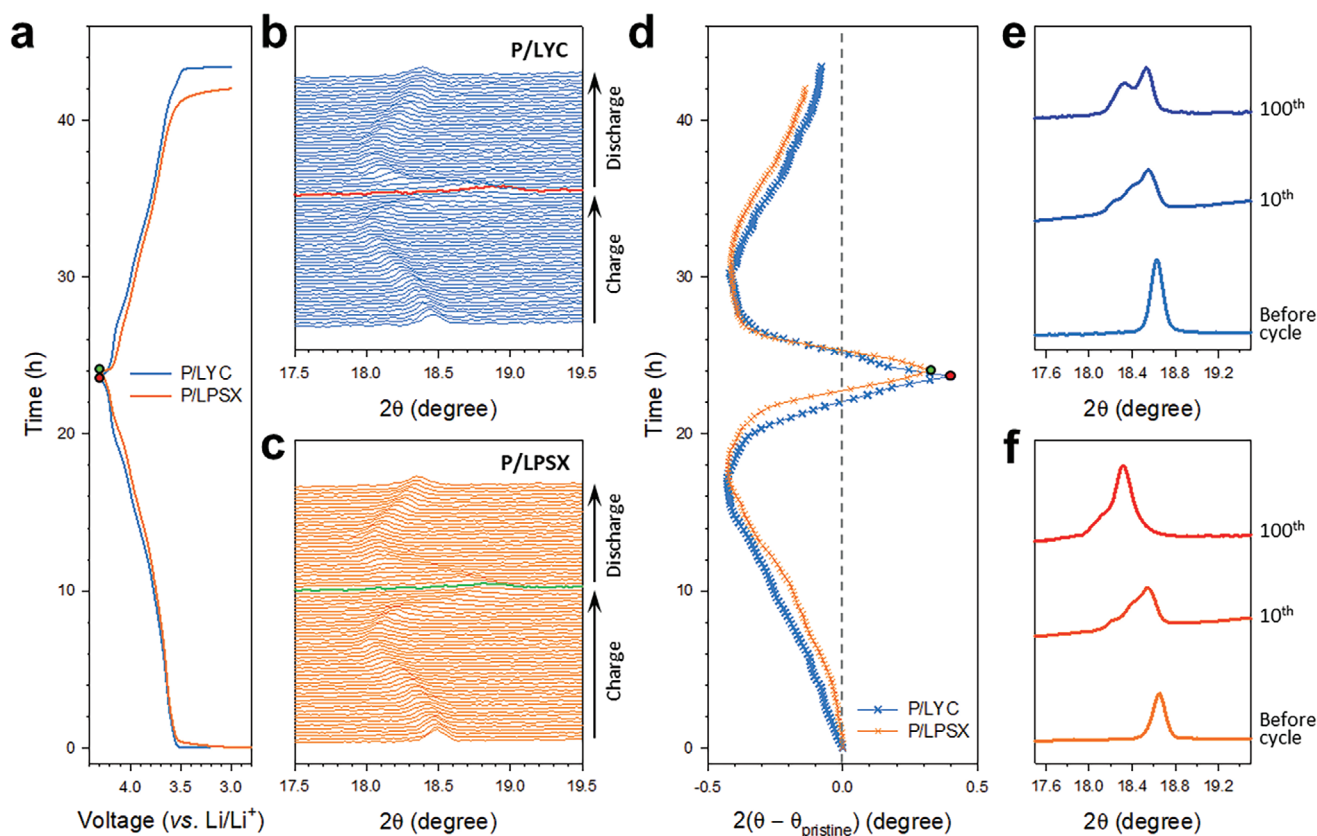

Figure 6. In situ and ex situ XRD results of the P/LYC and P/LPSX electrodes in all-solid-state cells cycled at room temperature. a) First charge–discharge voltage profiles of the P/LYC and P/LPSX electrodes and the corresponding XRD patterns showing the evolution of (003) peaks for b) P/LYC and c) P/LPSX. d) Corresponding changes in the (003) peak position, $2(\theta-\theta_{pristine})$. Full range in situ XRD patterns and corresponding lattice parameters are shown in Figure S24 in the Supporting Information. Ex situ XRD patterns showing the changes of (003) peaks before cycling and after cycling (at the 10th and 100th cycles) for e) P/LYC and f) P/LPSX.

for P/LYC. Moreover, at the end of charge, the overall (003) peak position change is smaller for P/LPSX than for P/LYC despite the slightly longer charging time (or higher charge capacity). Unambiguously, this result shows that Li$^+$ deintercalation from poly-NCA for the P/LPSX electrode was delayed, compared to the P/LYC electrode, which also agrees with the DEP results in Figure 5b and is indebted to the increased overpotential due to the side reaction of LPSX. Consequently, the lower SOC at the end of charge was observed. The more distinct internal cracks in poly-NCA after the first charge for the P/LYC electrode (Figure 2f) than for the P/LPSX electrode (Figure 2h) are thus understood. Similarly, the in situ XRD results indicate the lower depth-of-discharge (DOD) after the first discharge for the P/LPSX electrode than for the P/LYC electrode. Moreover, the ex situ XRD results showed a more significant negative shift in the (003) peak position after cycling for P/LPSX than for P/LYC (Figure 6e,f). This result is in accordance with the much poorer cycling performance of P/LPSX than that of P/LYC, which is associated with the severe LPSX-related side reaction. This side reaction not only causes an increase in the LPSX-NCA interfacial resistances, but also accelerates the pulverization of poly-NCA. Interestingly, the (003) peaks became broader and more asymmetric after cycling, which is indicative of largely varied SOCs of NCA particles in the electrodes.[78]

In summary, the complementary in situ and ex situ XRD analysis verified that Li$^+$ kinetics in and out of poly-NCA was retarded when combined with LPSX, which was accelerated upon repeated cycling. The underlying interfacial electrochemistry was probed by ex situ TEM and XPS for the electrodes cycled 100 times (**Figure 7**; Figures S27–S29, Supporting Information). TEM images and their corresponding fast Fourier transformed (FFT) patterns for P/LYC and P/LPSX are compared in Figure 7a,b, respectively. The poly-NCA particles in the P/LYC electrode did not show any difference in the crystal structure between the ii) core region and the i) surface region being in contact with SE LYC. In stark contrast, a ii) 20–30-nm thick surface layer that differs from a i) core region was observed for poly-NCA from the P/LPSX electrode and identified as the NiO-like rocksalt structure with a space group of Fm$\bar{3}$m. This is in good agreement with our previous results and could be interpreted as a consequence of the redox reaction between Ni^{4+} in NCA and sulfide SE LPSX.[37]

This reasoning is also well underpinned by the corresponding ex situ XPS results (Figure 7c,d) (the fitted results are summarized in Table S8 in the Supporting Information). For the electrode using LYC (P/LYC), both Y 3d and Cl 2p XPS signals showed no changes after cycling (Figure 7c), corroborating the intactness (or the excellent oxidation stability) of LYC, which in turn indicates no reaction with NCA. In contrast, the electrode using LPSX (P/LPSX) showed the significant evolution of the LPSX-derived oxidized species of bridging sulfur (P-[S]$_n$-P), P$_2$S$_5$, PO$_4^{3-}$, SO$_4^{2-}$,[37,42,46,66,75] which should be coupled by the formation of the rocksalt-like species from the original layered NCA.[37] Consistent results of ex situ TEM and ex situ XPS were also obtained for the electrodes using single-NCA (S/LYC and S/LPSX), as shown in Figures S27–S29 in the Supporting Information.

Finally, the cell performances of the four electrodes in our study were assessed in the multiple figures of merit and illustrated as a spider web diagram in **Figure 8**a (corresponding data are shown in Table S9 in the Supporting Information). The S/LYC electrode with 40.7 wt% LYC exhibited the highest ICE, rate capability, and cyclability, but at the expense of lowered energy density. Furthermore, the outstanding performances of all-solid-state cells, achieved by using cracking-free single-crystalline NCA and electrochemically oxidation-stable halide SE LYC, were compared with previous results of ASLBs in Figure 8b,c (the overall values are summarized in Table S10 in the Supporting Information). The capacity and cycling performance displayed are at the highest level for these despite the use of a high Ni content (88%).

3. Conclusions

In summary, the four electrodes using two types of NCAs (poly-NCA or single-NCA) and SEs (LYC or LPSX) for all-solid-state cells were complementarily analyzed via an arsenal of electrochemical, postmortem cross-sectional SEM-BSE, operando electrochemical pressiometry, in situ and ex situ XRD, ex situ TEM, and ex situ XPS measurements. Accordingly, the correlations between several important intercoupled factors (i.e., the density and size of particles, mechanical integrity of NCAs, and oxidation stability of SEs) and the electrochemical performances were revealed successfully. The corresponding electrochemo-mechanical and electrochemical evolution of the NCA electrodes are illustrated in **Figure 9**. Despite the structural integrity of single-NCA and the outstanding electrochemical oxidation stability of LYC, the S/LYC electrode suffered from the formation of internal cracks, which led to capacity fading upon cycling because of the small particle size of single-NCA and the heavy LYC. By increasing the amount of LYC sufficiently, from 29.1 to 40.7 wt%, the electrochemical performance of S/LYC was dramatically improved from 67.2% to 96.8% of the capacity retention at the 200th cycle. The severe side reaction occurring in LPSX, originating from the reactive Ni^{4+} and the oxidation-vulnerable sulfide, gives rise to impeded Li$^+$ transport at the interfaces (or interphases). Moreover, for the case of the P/LPSX electrode, it was disclosed that the additional localized volumetric strains caused by the side reaction of LPSX are responsible for the accelerated pulverization of the secondary particles in poly-NCA.

Our results provide important insights on the complex interfacial electrochemical and electrochemo-mechanical evolution of ASLBs. Several important research directions for advanced practical all-solid-state technology have been deduced. For the single-crystalline Ni-rich layered oxides, from the electrochemo-mechanical viewpoint, rigorous engineering is needed to control their morphology and particle size distribution in an economical way. In addition, the development of zero-strain cathode materials is important.[79] Employing "soft" Li$^+$ conductive binders also relieves the electrochemo-mechanical degradation.[18,38,80] Despite their excellent oxidation stability, most halide SEs (e.g., LYC) consist of heavy and expensive rare-earth elements.[60,66] Moreover, their Li$^+$ conductivity has remained at maximum 1–3 mS cm^{-1} (e.g., Li$_3$ScCl$_6$:[63] 3.0 mS cm^{-1}), which is approximately one order of magnitude lower than that of the state-of-the-art sulfide SEs (e.g., Li$_{9.54}$Si$_{1.74}$P$_{1.44}$S$_{11.7}$Cl$_{0.3}$:[5]
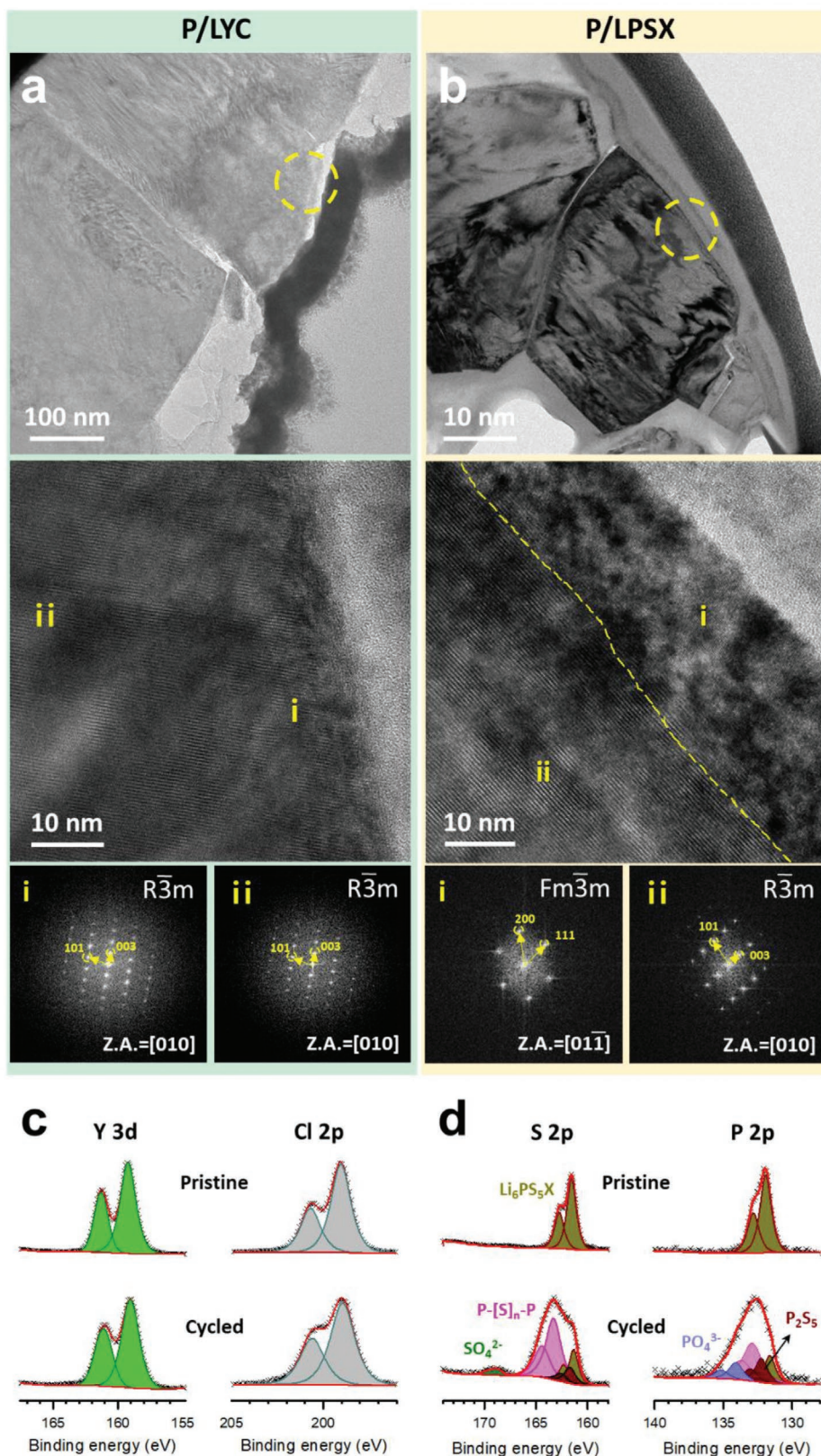
Figure 7. Ex situ TEM and XPS results of P/LYC and P/LPSX electrodes in all-solid-state cells cycled at room temperature. Low- and high-magnification ex situ TEM images for surface regions of the secondary particles of poly-NCA in contact with a) LYC and b) LPSX, and their corresponding FFT images. Ex situ XPS spectra for c) P/LYC and d) P/LPSX electrodes before cycling and after 100 cycles.
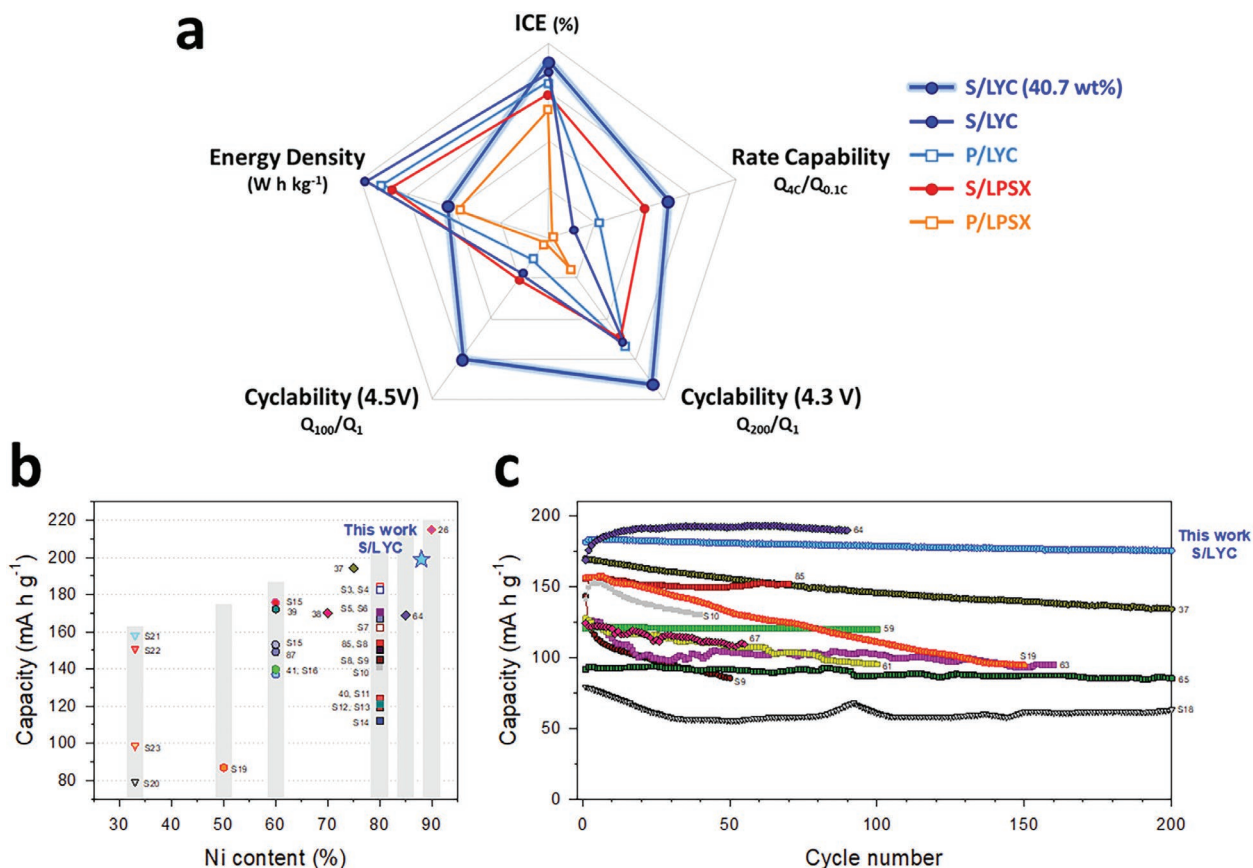
Figure 8. Comparison of the performances of NCA electrodes, varied by the type of NCAs (single- vs poly-crystalline) and SEs (halides (LYC) vs sulfides (LPSX)). a) Spider web diagram of cell performances for the NCA electrodes in terms of the ICE, rate capability, cyclability, and energy density. b) Discharge capacity and c) cycling performance for $LiCoO_2$ and Ni-rich layered oxides in all-solid-state cells. The vertical gray bars in (b) indicate the capacity of the liquid electrolyte cells.[88] Results using active cathode materials coated with buffering phases were excluded in (c).
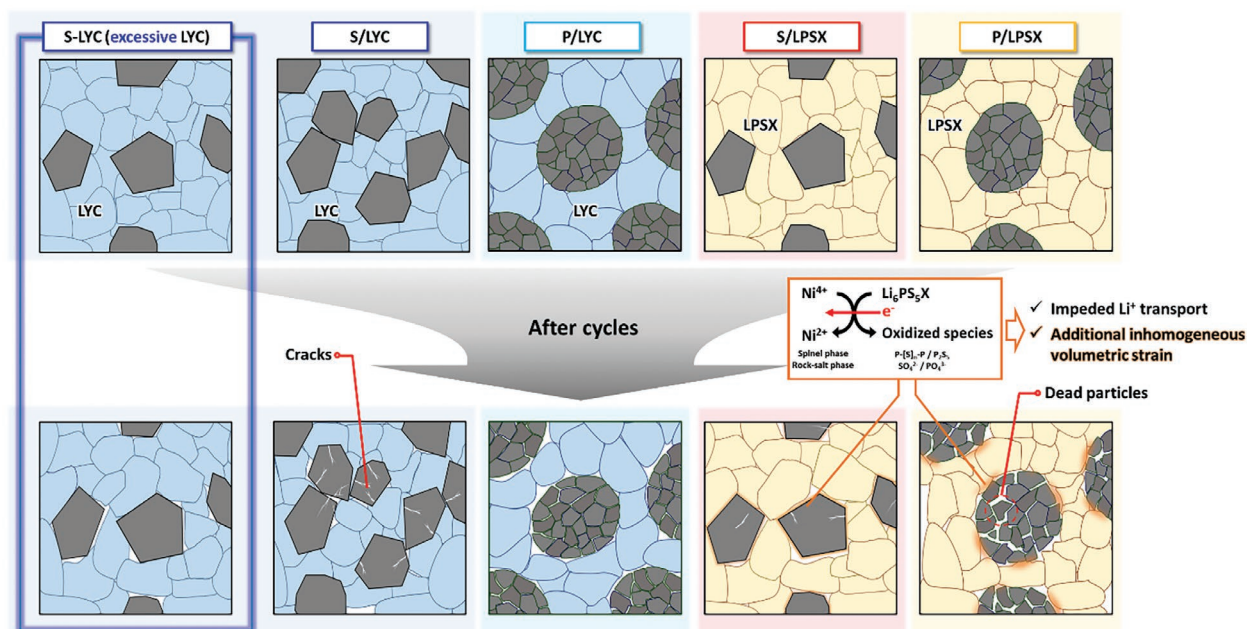

Figure 9. Schematic illustrating the different microstructural and interfacial evolutions in the NCA electrodes in all-solid-state cells, affected by the type of NCAs (single- vs poly-crystalline) and SEs (halides (LYC) vs sulfides (LPSX)).

**ADVANCED
SCIENCE NEWS**

www.advancedsciencenews.com

**ADVANCED
ENERGY
MATERIALS**

www.advenergymat.de

25 mS cm^{-1}) or conventional LEs (≥10 mS cm^{-1}). Indeed, the rate capability of the single-NCA electrodes could be significantly enhanced from 14.7% of capacity retention at 4C, compared to that at 0.1C, when using Li$_3$YCl$_6$ (0.40 mS cm^{-1}) to 39.4% by employing Li$_{2.7}$Y$_{0.7}$Zr$_{0.3}$Cl$_6$ with a higher conductivity of 1.1 mS cm^{-1} (Figure S30, Supporting Information).[65] Moreover, when subjected to cycling of up to 4.5 V (vs Li/Li$^+$), the S/LYC electrode, even with 40.7 wt% LYC, showed an unsatisfactory capacity retention of 75.1% at the 100th cycle (Figure S31, Supporting Information). As the majority of halide SEs identified thus far employs expensive central metals, such as rare earth metals and In, development using cost-effective central metals (e.g., Fe^{3+}-substituted Li$_2$ZrCl$_6$) is imperative for practical application.[66] Thus, the exploration or design of new halide SEs should be pursued by considering these aspects. Alternatively, the halide SEs could be utilized as functional interfacial layers between Ni-rich layered oxides and sulfide SEs, which could not only regulate the interfacial contacts but also protect them from undesirable side reactions of the sulfide SEs. In this regard, solution chemistry of halide SEs might be an interesting research direction.[8,14,81–85] Dry coating technologies could also be an alternative.[86,87]

4. Experimental Section

Preparation of Materials: Single- and poly-crystalline LiNi$_{0.88}$Co$_{0.11}$Al$_{0.01}$O$_2$ (NCA) powders were provided by EcoPro BM. Li$_6$PS$_5$Cl$_{0.5}$Br$_{0.5}$ (LPSX) powders were prepared by mechanochemical milling of a stoichiometric mixture of Li$_2$S (99.9%, Alfa Aesar), P$_2$S$_5$ (99%, Sigma Aldrich), LiCl (99.99%, Sigma Aldrich) and LiBr (99.99%, Sigma Aldrich) using Pulverisette 7 PL (Fritsch GmbH), and subsequent heat treatment in an Ar flow at 550 °C for 12 h. For the synthesis of Li$_3$YCl$_6$ powders, a stoichiometric mixture of LiCl (99.99%, Sigma Aldrich) and YCl$_3$ (99.99%, Sigma Aldrich) was ball-milled at 500 rpm for 20 h in a ZrO$_2$ vial with ZrO$_2$ balls. Nano-RuO$_2$ powders were purchased from Sigma Aldrich (<≈100 nm, 99.9%). Micro-RuO$_2$ powders (>≈1 μm) were prepared by sintering nano-RuO$_2$ powders at 1050 °C for 24 h in air.

Material Characterization: The chemical compositions of the NCA powders were determined by ICP-OES (OPTIMA 8300, Perkin Elmer). The particle size data for NCAs and SEs were collected by Laser Diffraction Particle Size Analyzer (Beckman Coulter) with dry and wet method. The surface areas of NCA powders were obtained by N$_2$ adsorption/desorption isotherms using Brunauer–Emmett–Teller (BET, 3 Flex, Micromeritics). Amounts of residual Li on surface of NCA were calculated by the Warder method, for which 0.1 M HCl solution and two indicators of phenolphthalein and methyl orange were used. Structural characterization of NCA and SE powders was performed by powder XRD measurements with Cu K$_\alpha$ radiation (1.5418 Å) using high-resolution X-ray diffractometer (Smartlab, Rigaku). The XRD data were collected between 10° and 110° with a step size of 0.02°, and analyzed by Rietveld refinement using Fullprof software. NCA/Li-In half cells were subjected to the in situ XRD measurements using a custom-made all-solid-state cell. The in situ XRD cells were charged and discharged between 3.0 and 4.3 V (vs Li/Li$^+$) by applying a constant current of 0.05C (9 mA g^{-1}). The in situ XRD data were continuously recorded in the range of 17–70° at a step width of 0.02° with Cu K$_\alpha$ radiation (1.5406 Å) using Rigaku MiniFlex 600 diffractometer. The in situ XRD cells were cycled under ≈1 MPa of an externally applied pressure. For ex situ XRD measurements, the electrodes collected after cycles were mounted on the holder and sealed with a Be window in an Ar-filled glove box. The ex situ XRD measurements were conducted using a Rigaku MiniFlex 600 diffractometer with Cu K$_\alpha$ radiation between 10 and 70° with a step size of 0.02°. SEM images of the NCA particles were obtained using a Verios G4UC (FEI). For cross-sectional SEM-BSE measurements, the electrodes were collected at different SOCs in an

Ar-filled glovebox and polished by Ar-ion beam milling using a cooling cross-sectional polisher (JEOL IB-19520CCP) at −100 °C. Then, the sample specimen was subjected to the SEM-BSE measurements. Exposure of the samples to atmospheric air was avoided by using an air-isolation system holder. For the quantitative analysis on the microcracks of poly-NCAs in the cross-sectional SEM-BSE images of the P/LYC and P/LPSX electrodes, the area fraction of the microcracks in poly-NCAs was obtained via "Adobe Photoshop" and "Image J" software programs, as illustrated in Figure 3a,b. Statistical values about the microcracks after first-cycle charge to 4.3 V (vs Li/Li$^+$), the subsequent discharge to 3.0 V (vs Li/Li$^+$), and after 100 cycles have been compiled in the boxplot (Figure 3c) and Table S5 (Supporting Information). For the ex situ TEM measurements, electrodes that were cycled 100 times at the discharged state (3 V vs Li/Li$^+$) were collected and cut into a 70 nm-thick thin foil using a focused ion beam (FIB, SCIOS, FEI) and loaded onto a Mo grid. The voltage of the ion beam was 30 kV and 5 kV for etching and cleaning, respectively. The ex situ XPS measurements were carried out with a monochromatic Al K$_\alpha$ source (1486.6 eV) at 12 kV and 6 mA using K-Alpha+ (Thermo Fisher Scientific). The samples were mounted on a sample holder in an Ar-filled glove box and transferred into the XPS equipment without any exposure to air.

Electrochemical Characterization: For the preparation of NCA electrodes in all-solid-state cells, a mixture of NCA (S-NCA or P-NCA), SE (LPSX or LYC), and conducting carbon additives (super C65) were dry-mixed in a weight ratio of 70:30:3 using mortar and pestle. The Li-In counter electrodes (or reference electrodes), which were partially lithiated indium (nominal composition of Li$_{0.5}$In), were prepared by mixing Li (FMC Lithium Corp.) and In (Aldrich, 99%) powders. All-solid-state cells with a diameter of 13 mm, comprised of Ti rods as the current collectors and polyaryletheretherketone (PEEK) mold, were assembled by the following procedure. After SE layers were formed by pelletizing 150 mg of LPSX powders (≈610 μm), the counter electrode (Li$_{0.5}$In) was placed on one side of the SE layer. After the as-prepared cathode mixture was spread on the other side of the SE layer, the assemblies were pressed at 370 MPa. The mass loading of the NCA electrodes was 11.3 mg cm^{-2}. For operando electrochemical pressiometry measurements using zero-strain Li$_4$Ti$_5$O$_{12}$ counter electrodes, pressure changes were monitored using a pressure sensor with a resolution of 0.1 kg (load cell, BONGSHIN). The Li$_4$Ti$_5$O$_{12}$ electrodes consist of Li$_4$Ti$_5$O$_{12}$, LPSX, and carbon (Super C65) in a weight ratio of 10.0:10.0:0.1. The electrode compositions for RuO$_2$ electrodes were RuO$_2$ and LPSX in a weight ratio of 41.6:58.4 and 78.1:21.9 for the micro- and nano-RuO$_2$ electrodes, respectively. 2032 coin cells were used for the test of liquid electrolyte cells. Composite electrodes consisting of S-NCA, super C65, and poly(vinylidene fluoride) in a weight ratio of 90:5.5:4.5 were prepared via casting N-methylpyrrolidone-based slurries on an Al foil and subsequent drying under vacuum at 120 °C. The electrode mass loading was 11 mg cm^{-2}. Celgard 2320 (Celgard) and Li metal were used as the separator and the counter (as well as reference) electrode, respectively. As a liquid electrolyte, 1 M LiPF$_6$ dissolved in ethylene carbonate, dimethyl carbonate, ethylmethyl carbonate in a vol. ratio of 3:4:3 with 10 wt% fluoroethylene carbonate was used. The liquid electrolyte cells were cycled at 0.5C (100 mA g^{-1}). The EIS measurements were performed for the cells discharged to 3.8 V (vs Li/Li$^+$) at 0.1C using a Bio-Logic (VMP3) from 1.5 MHz to 5 mHz with an amplitude of 10 mV. The external pressure of the all-solid-state cells during operation were ≈70 MPa.

Supporting Information

Supporting Information is available from the Wiley Online Library or from the author.

Conflict of Interest

The authors declare no conflict of interest.

Data Availability Statement

Research data are not shared.

Keywords

(electro)chemo-mechanical effects, halides, Ni-rich layered oxide cathodes, solid-state batteries, sulfides

[1] J. B. Goodenough, Y. Kim, *Chem. Mater.* **2010**, *22*, 587.
[2] J. W. Choi, D. Aurbach, *Nat. Rev. Mater.* **2016**, *1*, 1.
[3] X. B. Cheng, R. Zhang, C. Z. Zhao, Q. Zhang, *Chem. Rev.* **2017**, *117*, 10403.
[4] K. Liu, Y. Liu, D. Lin, A. Pei, Y. Cui, *Sci. Adv.* **2018**, *4*, eaas9820.
[5] Y. Kato, S. Hori, T. Saito, K. Suzuki, M. Hirayama, A. Mitsui, M. Yonemura, H. Iba, R. Kanno, *Nat. Energy* **2016**, *1*, 16030.
[6] K. Kerman, A. Luntz, V. Viswanathan, Y.-M. Chiang, Z. Chen, *J. Electrochem. Soc.* **2017**, *164*, A1731.
[7] Z. Zhang, Y. Shao, B. Lotsch, Y.-S. Hu, H. Li, J. Janek, L. F. Nazar, C. Nan, J. Maier, M. Armand, L. Chen, *Energy Environ. Sci.* **2018**, *11*, 1945.
[8] K. H. Park, Q. Bai, D. H. Kim, D. Y. Oh, Y. Zhu, Y. Mo, Y. S. Jung, *Adv. Energy Mater.* **2018**, *8*, 1800035.
[9] X. Han, Y. Gong, K. K. Fu, X. He, G. T. Hitz, J. Dai, A. Pearse, B. Liu, H. Wang, G. Rubloff, Y. Mo, V. Thangadurai, E. D. Wachsman, L. Hu, *Nat. Mater.* **2017**, *16*, 572.
[10] R. Chen, Q. Li, X. Yu, L. Chen, H. Li, *Chem. Rev.* **2020**, *120*, 6820.
[11] H. J. Deiseroth, S. T. Kong, H. Eckert, J. Vannahme, C. Reiner, T. Zaiss, M. Schlosser, *Angew. Chem., Int. Ed.* **2008**, *47*, 755.
[12] P. Adeli, J. D. Bazak, K. H. Park, I. Kochetkov, A. Huq, G. R. Goward, L. F. Nazar, *Angew. Chem., Int. Ed.* **2019**, *58*, 8681.
[13] K. Xu, *Chem. Rev.* **2004**, *104*, 4303.
[14] K. H. Park, D. Y. Oh, Y. E. Choi, Y. J. Nam, L. Han, J.-Y. Kim, H. Xin, F. Lin, S. M. Oh, Y. S. Jung, *Adv. Mater.* **2016**, *28*, 1874.
[15] W. D. Richards, L. J. Miara, Y. Wang, J. C. Kim, G. Ceder, *Chem. Mater.* **2016**, *28*, 266.
[16] S. Wang, H. Xu, W. Li, A. Dolocan, A. Manthiram, *J. Am. Chem. Soc.* **2018**, *140*, 250.
[17] D. Y. Oh, Y. J. Nam, K. H. Park, S. H. Jung, S.-J. Cho, Y. K. Kim, Y.-G. Lee, S.-Y. Lee, Y. S. Jung, *Adv. Energy Mater.* **2015**, *5*, 1500865.
[18] D. Y. Oh, Y. J. Nam, K. H. Park, S. H. Jung, K. T. Kim, A. R. Ha, Y. S. Jung, *Adv. Energy Mater.* **2019**, *9*, 1802927.
[19] H. Muramatsu, A. Hayashi, T. Ohtomo, S. Hama, M. Tatsumisago, *Solid State Ionics* **2011**, *182*, 116.
[20] Y. Zhu, Y. Mo, *Angew. Chem. Int. Ed.* **2020**, *59*, 17472.
[21] B. R. Shin, Y. J. Nam, D. Y. Oh, D. H. Kim, J. W. Kim, Y. S. Jung, *Electrochim. Acta* **2014**, *146*, 395.
[22] Y. Zhu, X. He, Y. Mo, *ACS Appl. Mater. Interfaces* **2015**, *7*, 23685.
[23] P. Albertus, S. Babinec, S. Litzelman, A. Newman, *Nat. Energy* **2018**, *3*, 16.
[24] T. Krauskopf, F. H. Richter, W. G. Zeier, J. Janek, *Chem. Rev.* **2020**, *120*, 7745.
[25] Y. Chen, Z. Wang, X. Li, X. Yao, C. Wang, Y. Li, W. Xue, D. Yu, S. Y. Kim, F. Yang, A. Kushima, G. Zhang, H. Huang, N. Wu, Y.-W. Mai, J. B. Goodenough, J. Li, *Nature* **2020**, *578*, 251.
[26] Y.-G. Lee, S. Fujiki, C. Jung, N. Suzuki, N. Yashiro, R. Omoda, D.-S. Ko, T. Shiratsuchi, T. Sugimoto, S. Ryu, J. H. Ku, T. Watanabe, Y. Park, Y. Aihara, D. Im, I. T. Han, *Nat. Energy* **2020**, *5*, 299.
[27] F. Han, A. S. Westover, J. Yue, X. Fan, F. Wang, M. Chi, D. N. Leonard, N. J. Dudney, H. Wang, C. Wang, *Nat. Energy* **2019**, *4*, 187.
[28] G. Cui, *Matter* **2020**, *2*, 805.
[29] M. J. Wang, E. Carmona, A. Gupta, P. Albertus, J. Sakamoto, *Nat. Commun.* **2020**, *11*, 5201.
[30] J. R. Dahn, U. Vonsacken, C. A. Michal, *Solid State Ionics* **1990**, *44*, 87.
[31] J. Kim, H. Lee, H. Cha, M. Yoon, M. Park, J. Cho, *Adv. Energy Mater.* **2018**, *8*, 1702028.
[32] K.-J. Park, J.-Y. Hwang, H.-H. Ryu, F. Maglia, S.-J. Kim, P. Lamp, C. S. Yoon, Y.-K. Sun, *ACS Energy Lett.* **2019**, *4*, 1394.
[33] W. Lee, S. Muhammad, C. Sergey, H. Lee, J. Yoon, Y. Kang, W. Yoon, *Angew. Chem., Int. Ed.* **2019**, *58*, 2.
[34] M. Bianchini, M. Roca-Ayats, P. Hartmann, T. Brezesinski, J. Janek, *Angew. Chem., Int. Ed.* **2018**, *58*, 10434.
[35] F. Lin, D. Nordlund, I. M. Markus, T.-C. Weng, H. L. Xin, M. M. Doeff, *Energy Environ. Sci.* **2014**, *7*, 3077.
[36] L. Zou, W. Zhao, Z. Liu, H. Jia, J. Zheng, G. Wang, Y. Yang, J.-G. Zhang, C. Wang, *ACS Energy Lett.* **2018**, *3*, 2433.
[37] S. H. Jung, U. H. Kim, J. H. Kim, S. Jun, C. S. Yoon, Y. S. Jung, Y. K. Sun, *Adv. Energy Mater.* **2020**, *10*, 1903360.
[38] D. Y. Oh, K. T. Kim, S. H. Jung, D. H. Kim, S. Jun, S. Jeoung, H. R. Moon, Y. S. Jung, *Mater. Today* **2021**, https://doi.org/10.1016/j.mattod.2021.01.006.
[39] D. Y. Oh, D. H. Kim, S. H. Jung, J.-G. Han, N.-S. Choi, Y. S. Jung, *J. Mater. Chem. A* **2017**, *5*, 20771.
[40] R. Koerver, I. Aygün, T. Leichtweiß, C. Dietrich, W. Zhang, J. O. Binder, P. Hartmann, W. G. Zeier, J. r. Janek, *Chem. Mater.* **2017**, *29*, 5574.
[41] Y. J. Nam, K. H. Park, D. Y. Oh, W. H. An, Y. S. Jung, *J. Mater. Chem. A* **2018**, *6*, 14867.
[42] J. Auvergniot, A. Cassel, J. B. Ledeuil, V. Viallet, V. Seznec, R. Dedryvere, *Chem. Mater.* **2017**, *29*, 3883.
[43] A. Banerjee, X. Wang, C. Fang, E. A. Wu, Y. S. Meng, *Chem. Rev.* **2020**, *120*, 6878.
[44] F. Walther, R. Koerver, T. Fuchs, S. Ohno, J. Sann, M. Rohnke, W. G. Zeier, J. Janek, *Chem. Mater.* **2019**, *31*, 3745.
[45] N. Ohta, K. Takada, L. Zhang, R. Ma, M. Osada, T. Sasaki, *Adv. Mater.* **2006**, *18*, 2226.
[46] S. H. Jung, K. Oh, Y. J. Nam, D. Y. Oh, P. Brüner, K. Kang, Y. S. Jung, *Chem. Mater.* **2018**, *30*, 8190.
[47] X. Xu, K. Takada, T. Fukuda, T. Ohnishi, K. Akatsuka, M. Osada, B. T. Hang, K. Kumagai, T. Sekiguchi, T. Sasaki, *Energy Environ. Sci.* **2011**, *4*, 3509.
[48] J. H. Woo, J. J. Travis, S. M. George, S.-H. Lee, *J. Electrochem. Soc.* **2015**, *162*, A344.
[49] W. Zhang, T. Leichtweiß, S. P. Culver, R. Koerver, D. Das, D. A. Weber, W. G. Zeier, J. Janek, *ACS Appl. Mater. Interfaces* **2017**, *9*, 35888.
[50] R. Koerver, W. Zhang, L. de Biasi, S. Schweidler, A. Kondrakov, S. Kolling, T. Brezesinski, P. Hartmann, W. Zeier, J. Janek, *Energy Environ. Sci.* **2018**, *11*, 2142.
[51] S. Jun, Y. J. Nam, H. Kwak, K. T. Kim, D. Y. Oh, Y. S. Jung, *Adv. Funct. Mater.* **2020**, *30*, 2002535.

[52] A. O. Kondrakov, A. Schmidt, J. Xu, H. Geßwein, R. Mönig, P. Hartmann, H. Sommer, T. Brezesinski, J. Janek, *J. Phys. Chem. C* **2017**, *121*, 3286.

[53] X. Fan, G. Hu, B. Zhang, X. Ou, J. Zhang, W. Zhao, H. Jia, L. Zou, P. Li, Y. Yang, *Nano Energy* **2020**, *70*, 104450.

[54] G. Qian, Y. Zhang, L. Li, R. Zhang, J. Xu, Z. Cheng, S. Xie, H. Wang, Q. Rao, Y. He, Y. Shen, L. Chen, M. Tang, Z.-F. Ma, *Energy Storage Mater.* **2020**, *27*, 140.

[55] F. Zhang, S. Lou, S. Li, Z. Yu, Q. Liu, A. Dai, C. Cao, M. F. Toney, M. Ge, X. Xiao, W. K. Lee, Y. Yao, J. Deng, T. Liu, Y. Tang, Y. Gin, J. Lu, D. Su, J. Wang, *Nat. Commun.* **2020**, *11*, 3050.

[56] H. Li, J. Li, N. Zaker, N. Zhang, G. A. Botton, J. R. Dahn, *J. Electrochem. Soc.* **2019**, *166*, A1956.

[57] Y. Bi, J. Tao, Y. Wu, L. Li, Y. Xu, E. Hu, B. Wu, J. Hu, C. Wang, J. G. Zhang, Y. Qi, J. Xiao, *Science* **2020**, *370*, 1313.

[58] H. Cha, J. Kim, H. Lee, N. Kim, J. Hwang, J. Sung, M. Yoon, K. Kim, J. Cho, *Adv. Mater.* **2020**, *32*, 2003040.

[59] T. Asano, A. Sakai, S. Ouchi, M. Sakaida, A. Miyazaki, S. Hasegawa, *Adv. Mater.* **2018**, *30*, 1803075.

[60] X. Li, J. Liang, X. Yang, K. R. Adair, C. Wang, F. Zhao, X. Sun, *Energy Environ. Sci.* **2020**, *13*, 1429.

[61] X. Li, J. Liang, J. Luo, M. Norouzi Banis, C. Wang, W. Li, S. Deng, C. Yu, F. Zhao, Y. Hu, T.-K. Sham, L. Zhang, S. Zhao, S. Lu, H. Huang, R. Li, K. R. Adair, X. Sun, *Energy Environ. Sci.* **2019**, *12*, 2665.

[62] S. Muy, J. Voss, R. Schlem, R. Koerver, S. J. Sedlmaier, F. Maglia, P. Lamp, W. G. Zeier, Y. Shao-Horn, *iScience* **2019**, *16*, 270.

[63] J. Liang, X. Li, S. Wang, K. R. Adair, W. Li, Y. Zhao, C. Wang, Y. Hu, L. Zhang, S. Zhao, S. Lu, H. Huang, R. Li, Y. Mo, X. Sun, *J. Am. Chem. Soc.* **2020**, *15*, 7012.

[64] L. Zhou, C. Y. Kwok, A. Shyamsunder, Q. Zhang, X. Wu, L. F. Nazar, *Energy Environ. Sci.* **2020**, *13*, 2056.

[65] K.-H. Park, K. Kaup, A. Assoud, Q. Zhang, X. Wu, L. F. Nazar, *ACS Energy Lett.* **2020**, *5*, 533.

[66] H. Kwak, D. Han, J. Lyoo, J. Park, S. H. Jung, Y. Han, G. Kwon, H. Kim, S. T. Hong, K. W. Nam, Y. S. Jung, *Adv. Energy Mater.* **2021**, 2003190.

[67] Z. Liu, S. Ma, J. Liu, S. Xiong, Y. Ma, H. Chen, *ACS Energy Lett.* **2021**, *6*, 298.

[68] W. M. Seong, K. H. Cho, J. W. Park, H. Park, D. Eum, M. H. Lee, I. S. Kim, J. Lim, K. Kang, *Angew. Chem., Int. Ed.* **2020**, *59*, 18662.

[69] T. Shi, Q. Tu, Y. Tian, Y. Xiao, L. J. Miara, O. Kononova, G. Ceder, *Adv. Energy Mater.* **2019**, *10*, 1902881.

[70] C. Zhu, R. E. Usiskin, Y. Yu, J. Maier, *Science* **2017**, *358*, 1400.

[71] F. P. McGrogan, T. Swamy, S. R. Bishop, E. Eggleton, L. Porz, X. Chen, Y. Chiang, K. J. V. Vliet, *Adv. Energy Mater.* **2017**, *7*, 1602011.

[72] Y. S. Jung, P. Lu, A. S. Cavanagh, C. Ban, G. H. Kim, S. H. Lee, S. M. George, S. J. Harris, A. C. Dillon, *Adv. Energy Mater.* **2013**, *3*, 213.

[73] T. Ohzuku, T. Sawai, T. Hirai, *J. Electrochem. Soc.* **1990**, *137*, 3004.

[74] S. H. Jung, D. H. Kim, P. Brüner, H. Lee, H. J. Hah, S. K. Kim, Y. S. Jung, *Electrochim. Acta* **2017**, *232*, 236.

[75] T. Hakari, M. Deguchi, K. Mitsuhara, T. Ohta, K. Saito, Y. Orikasa, Y. Uchimoto, Y. Kowada, A. Hayashi, M. Tatsumisago, *Chem. Mater.* **2017**, *29*, 4768.

[76] C. Ghanty, B. Markovsky, E. M. Erickson, M. Talianker, O. Haik, Y. Tal-Yossef, A. Mor, D. Aurbach, J. Lampert, A. Volkov, J.-Y. Shin, A. Garsuch, F. F. Chesneau, C. Erk, *ChemElectroChem* **2015**, *2*, 1479.

[77] J. Li, R. Shunmugasundaram, R. Doig, J. R. Dahn, *Chem. Mater.* **2015**, *28*, 162.

[78] T. Bartsch, A. Y. Kim, F. Strauss, L. de Biasi, J. H. Teo, J. Janek, P. Hartmann, T. Brezesinski, *Chem. Commun.* **2019**, *55*, 11223.

[79] F. Strauss, L. Biasi, A. Y. Kim, J. Hertle, S. Schweidler, J. Janek, P. Hartmann, T. Brezesinski, *ACS Mater. Lett.* **2020**, *2*, 84.

[80] K. T. Kim, D. Y. Oh, S. Jun, Y. B. Song, T. Y. Kwon, Y. Han, Y. S. Jung, *Adv. Energy Mater.* **2021**, 2003766.

[81] A. Banerjee, K. H. Park, J. W. Heo, Y. J. Nam, C. K. Moon, S. M. Oh, S. T. Hong, Y. S. Jung, *Angew. Chem.* **2016**, *55*, 9634.

[82] L. Duchene, R. S. Kuhnel, E. Stilp, E. Cuervo Reyes, A. Remhof, H. Hagemann, C. Battaglia, *Energy Environ. Sci.* **2017**, *10*, 2609.

[83] D. H. Kim, Y.-H. Lee, Y. B. Song, H. Kwak, S.-Y. Lee, Y. S. Jung, *ACS Energy Lett.* **2020**, *5*, 718.

[84] Y. B. Song, D. H. Kim, H. Kwak, D. Han, S. Kang, J. H. Lee, S. M. Bak, K. W. Nam, H. W. Lee, Y. S. Jung, *Nano Lett.* **2020**, *20*, 4337.

[85] X. Li, J. Liang, N. Chen, J. Luo, K. R. Adair, C. Wang, M. N. Banis, T. K. Sham, L. Zhang, S. Zhao, S. Lu, H. Huang, R. Li, X. Sun, *Angew. Chem., Int. Ed.* **2019**, *58*, 16427.

[86] H. Nakamura, T. Kawaguchi, T. Masuyama, A. Sakuda, T. Saito, K. Kuratani, S. Ohsaki, S. Watano, *J. Power Sources* **2020**, *448*, 227579.

[87] Y. J. Nam, D. Y. Oh, S. H. Jung, Y. S. Jung, *J. Power Sources* **2018**, *375*, 93.

[88] C. S. Yoon, K.-J. Park, U.-H. Kim, K. H. Kang, H.-H. Ryu, Y.-K. Sun, *Chem. Mater.* **2017**, *29*, 10436.